Geophys. J. R. astr. Soc. (1987) **91**, 57–71

The Ancash, Peru, earthquake of 1946 November 10: evidence for low-angle normal faulting in the high Andes of northern Peru

Diane I. Doser *Department of Geological Sciences, University of Texas at El Paso, El Paso, Texas 79968-0555, USA*

Accepted 1987 February 23. Received 1987 February 20; in original form 1986 September 23

Summary. The Ancash, Peru, earthquake is the largest and best documented intracontinental normal-fault earthquake to have occurred in historically recorded time along the Andean margin of South America. The fault geometry and the rupture processes of this earthquake provide information on how normal faulting develops in a predominantly compressional regime, and on the hazards associated with normal faulting in other parts of the Andes. A re-evaluation of first-motion data, intensity data, and epicentre locations, coupled with waveform modelling, suggests that the earthquake occurred along a fault that dips $30^\circ \pm 10^\circ$ at a hypocentral depth of 15–17 km. Geological information also suggests that the earthquake reactivated an older thrust fault that was favourably orientated with respect to the present regional stress regime.

Key words: earthquake parameters, normal faulting, northern Peru tectonics

1 Introduction

The Andean continental margin of South America is often considered to be analogous to the western margin of North America during Late Cretaceous and Early Tertiary time (Burchfiel & Davis 1972, 1975) when the Farallon plate was being subducted beneath North America. Although the Andean margin is a compressional regime where thrust- and reverse-faulting predominate, young normal faults exist in a number of localities in the high Andes. Study of these intracontinental normal faults may give us insight into how extensional faulting was initiated in western North America, leading to the development of the Basin and Range province, and how present-day normal faulting in the western United States may differ from the youthful faulting in the high Andes.

Quaternary age normal faults have been recognized in the Cordillera Blanca of central Peru (Yonekura *et al.* 1979; Dalmayrac & Molnar 1981; Schwartz *et al.* 1984) and the Altiplano of southern Peru (Fig. 1) (Mercier 1981; Suárez, Molnar & Burchfiel 1983), however, the only earthquake that has been documented to have occurred along a normal fault is the Ancash, Peru, earthquake of 1946 November 10. The earthquake produced

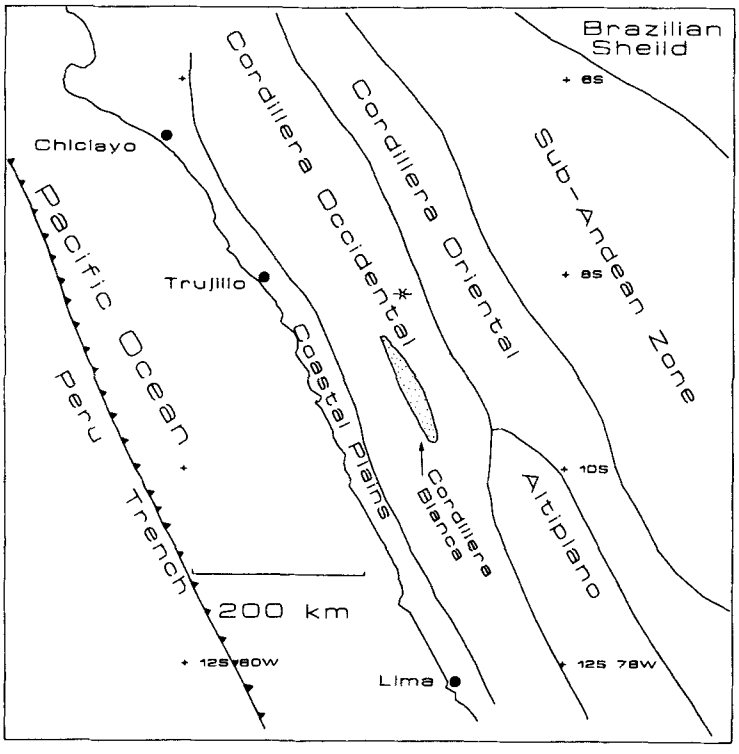

Figure 1. Physiographic provinces of the central Andes region. Asterisk shows location of the Ancash, Peru, earthquake. Stippled region is the Cordillera Blanca. Dots indicate cities.

surface faulting and was large enough to be well-recorded at teleseismic distances. This study seeks to determine the geometry of faulting during this earthquake and its relationship to older thrust faults in the region. I achieve this goal by re-examining previous studies of first-motion data, intensity distribution, and epicentre relocations, and by modelling teleseismic body waveforms.

I compare surface faulting in the Ancash earthquake with other areas of normal faulting in the Andes to determine whether the Ancash event is representative of the style of extensional deformation seen throughout the Andes. I also compare the results with observations of normal-fault earthquakes in the western United States and the Aegean region.

2 Geologic setting

The Ancash earthquake occurred in north-central Peru on a high terrace (4000 m) between the continental divide and the Marañón River (Fig. 2) on the north-eastern edge of the Cordillera Occidental physiographic province (Fig. 1). It is a region of rugged topography characterized by deep V-shaped valleys with stream gradients of 200 m km^{-1}. The region lies about 50 km east of the Coastal Batholith in an area whose local geology is similar to that of a foreland fold and thrust belt (Fig. 2). Heim (1949), Cobbing (1973), and Wilson, Reyes & Garayar (1967) show that Cretaceous limestones in the region have been thrust eastwards over west-dipping faults (Fig. 3). The underlying Jurassic shales have been tightly folded. The age of the deformation has been estimated to be Late Cretaceous to Early Cenozoic

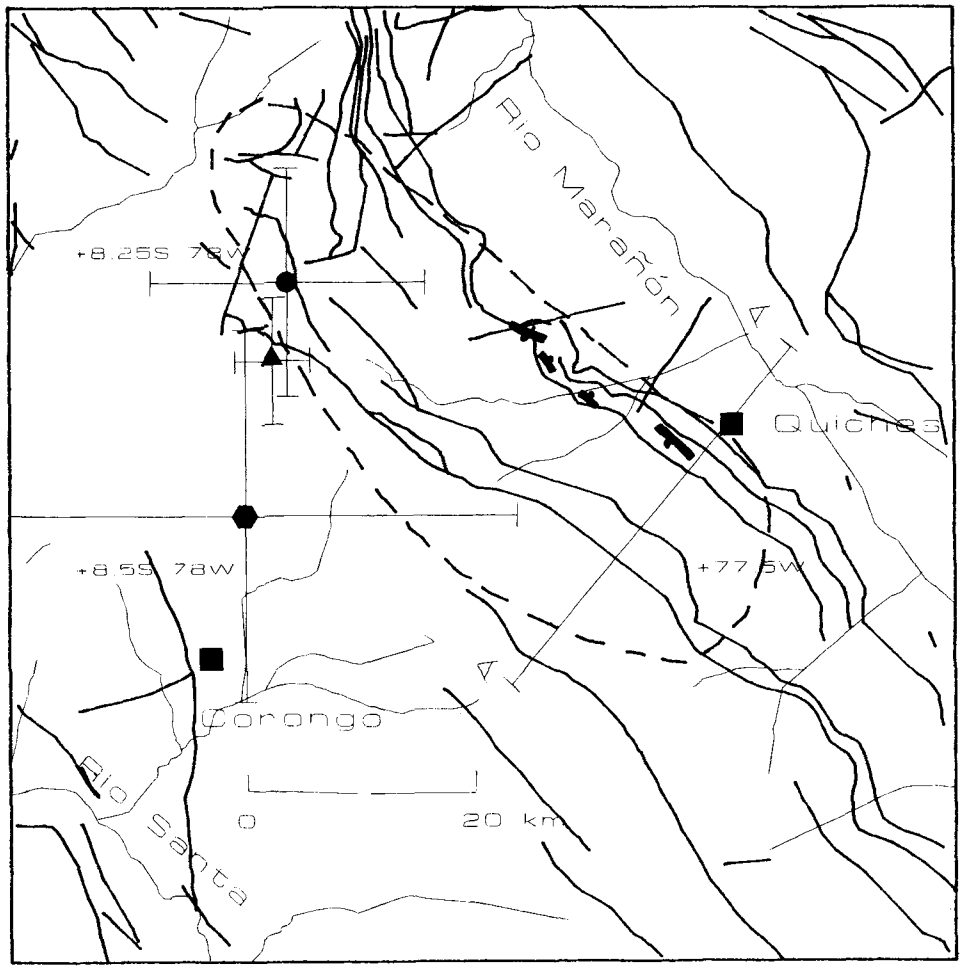

Figure 2. Faulting in the Ancash region. Thick lines are thrust faults modified from Cobbing (1973). Thin lines indicate rivers. The boldest lines represent surface faulting during 1946 with balls indicating the downthrown side of the faults. The dashed line encloses the isoseismal area of intensity 8 or greater. The circle and triangle represent the earthquake locations of Silgado (1951). Silgado does not indicate how the error bars for these locations were obtained. The hexagon represents the relocation determined in this study. The error bars for this location show the 95 per cent confidence interval (Flinn 1965). The squares represent towns. A cross-section along A–A′ is shown in Fig. 3.

since Oligocene–Miocene volcanic rocks lie unconformably over the deformed Cretaceous limestones (Wilson *et al.* 1967).

Surface faulting produced during the earthquake is shown in Fig. 2. Mapping of the surface faulting began three days after the earthquake (Silgado 1951) but was not completed until nearly a year later. The rugged topography of the region hindered mapping, and the lack of geodetic control precluded measurement of the direction or amount of absolute surface movement during the earthquake. Silgado (1951) also records only the maximum measured offsets for separate fault segments in his report, so it is not possible to estimate the average slip along the fault zone or the change in offset along strike. Surface faulting was discontinuous with an overall strike of about N40–50°W.

The southernmost fault segment was 5 km long with a strike of N42°W and a maximum

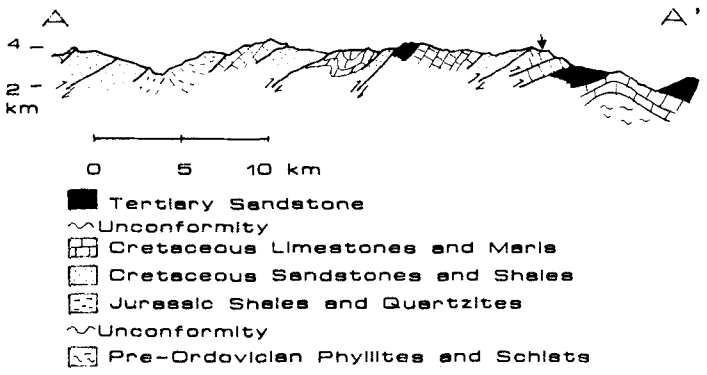

Figure 3. Geologic cross-section along A–A′ (Fig. 2) from Heim (1949). The bold arrow denotes the location of 1946 fault scarp.

dip of 58°SW. Silgado does not state whether this dip measurement was made in near-surface alluvium or bedrock. A finely polished limestone surface along this segment of the fault, however, was observed to dip 42°SW. Striations along the fault plane indicate that displacement was pure dip-slip. A maximum slip of 3.5 m in alluvial material was measured along this segment. The effect of distortion in the manner of graben formation, backtilting or the compaction of the alluvial material was not considered in this measurement of displacement. The surface faulting dies out towards the north-west before reaching a deep canyon.

About 12 km further north-west the scarp reappears for another 3 km. This short segment has a maximum displacement of 1 m and cuts across quartzites at a strike of N55°W. A set of fractures in limestone 2 km to the west parallel the main fault to form a graben about 2 km wide. The longest fracture extends for 2 km with a strike of N40°W and dip of 30°NE with a maximum displacement of 1 m.

Fig. 2 shows that the main fault scarp closely parallels mapped older thrust faults. The arrow in Fig. 3 shows the location of the surface faulting with respect to the older thrust faults. The main scarp dips to the south-west, the dip direction of the older thrusts, and one scarp in bedrock was measured to dip 42° at the surface, a value only slightly larger than the 25°–35° dips of the older thrust sheets at the surface (Heim 1949). The discontinuous nature of the surface faulting may be controlled in part by the topography; however, the fault map (Fig. 2) indicates that the segmentation may also be controlled by the presence of older cross-faults. Note that the north-eastern footwall block does not form a prominent topographical high (Fig. 3). Lack of major topographical expression of the footwall block suggests that normal faulting in the region is either a very recent feature and/or occurs at a slower rate than erosion. Photographs of the surface faulting (Silgado 1951) show evidence for at least one normal fault event of comparable displacement prior to 1946 (D. P. Schwartz private communication).

3 Previous seismic studies

The Ancash region of Peru is part of the Andean margin where the Nazca plate is undergoing subduction at a shallow dip of 10°–15° (Stauder 1975). The majority of seismicity along this part of the Andes is confined to two zones, one along the trench and the other in the region between the Cordillera Oriental and the Sub-Andes (Fig. 1) (Suárez *et al.* 1983). There has been a noteable lack of seismicity in the high Andes (Suárez *et al.* 1983).

The quoted magnitude for the Ancash earthquake is 7¼ (Silgado 1951; Richter 1958). About 1400 people were killed during the earthquake sequence, 500 from landslides that had an estimated total volume of 2×10^6 m^3 (Silgado 1951). One city was completely buried by landslides, and in Quiches (Fig. 2) 95 per cent of the buildings were completely destroyed or rendered uninhabitable (Silgado 1951).

Silgado (1951) collected intensity data from three days to a year after the earthquake and plotted an intensity map of part of the region. This map is presented in Fig. 4. It should be noted that intensity information north-east of the earthquake is sparse. When Silgado determined intensities he relied more heavily on topographical changes, landslides, and other secondary effects, than on building damage, because construction practices in the region are different from those upon which the Modified Mercalli scale is based.

The shape of the isoseismals in the epicentral region (Fig. 2) suggests that the fault scarp dipping to the south-west is the main fault scarp, but the shape could be a topographic effect controlled by the steep gorge of the Marañón river to the east of the fault. The isoseismal shape also seems to suggest that the rupture may have begun along the south-eastern end of the fault and propagated to the north-west. This agrees with the observation that the maximum displacement along the fault occurred near Quiches and that displacement decreased north-westward, although the local geology, again, may influence the shape of the isoseismals.

If attenuation in the Ancash region is comparable to that in western United States, then the area of Modified Mercalli intensity VI or greater for the Ancash earthquake is

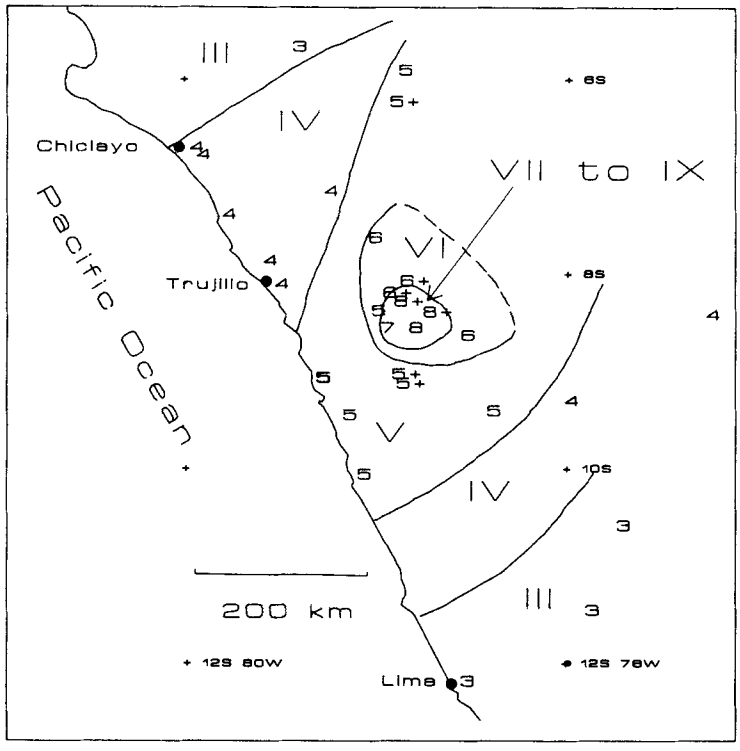

Figure 4. Intensity map of the Ancash earthquake based on Silgado's (1951) intensity measurements. Each Arabic numeral represents an individual intensity measurement. The Roman numerals identify separate isoseismal zones.

Table 1. Magnitudes and isoseismal areas of normal-fault earthquakes

Earthquake	Magnitude	Area of intensity > VI ($\times 10^{14}$ cm^2)	Reference
Ancash, Peru 1946 November 10	7¼	5.0	This study
Pleasant Valley, Nevada 1915 October 2	7¾	12.4	Richter (1958)
Valentine, Texas 1931 August 16	6.4	6.0	Sanford & Topozada (1974)
Fallon, Nevada 1954 July 6	6.1(M_S)	5.0	Cloud (1956)
Fallon, Nevada 1954 August 24	6.5(M_S)	8.0	Cloud (1956)
Hebgen Lake, Montana 1959 August 18	7.5(M_S)	16.0	Steinbrugge & Cloud (1962)
Borah Peak, Idaho 1985 October 28	7.3(M_S)	5.5	Stover (1985)

comparable to a magnitude 6–7 earthquake in the western United States (Table 1). The disparity between this magnitude value and previous values of 7¼ prompted a redetermination of the earthquake's magnitude. I obtained estimates that ranged from 6.3 to 6.5 for M_S and from 6.5 to 6.9 for m_b, magnitude values similar to those suggested by the dimensions of the isoseismal area.

Silgado (1951) located the Ancash earthquake using 11 stations located in South and North America. His initial location (8°16.2′ ± 5.4′S, 77°49.6′ ± 6.5′W; circle in Fig. 2) was about 30 km west-north-west of the northernmost surface faulting, suggesting unilateral rupture to the south-east during the earthquake. His second relocation (8°19.9′ ± 3.0′S, 77°50.3′ ± 1.8′W; triangle in Fig. 2) placed the epicentre 30 km west of the northernmost surface faulting. Although Silgado obtained error bars for the locations (Fig. 2), he did not state how these errors were determined, or what confidence level they represented. Therefore, I attempted a relocation using Silgado's *P*-wave arrival times and a Jeffreys–Bullen earth model. I obtained a solution (8°28.4′S, 77°51.6′W; hexagon in Fig. 2) located 15–25 km south of Silgado's locations, but with a 95 per cent confidence interval (Flinn 1965) that would span the entire fault zone. This indicates that the epicentre location should not be used to evaluate direction of rupture propagation.

Silgado estimated the focal depth of this earthquake to be 30–40 km based on his measurement of the *pP–P* interval. Hodgson & Bremner (1953) estimated a depth of 27 km based on the felt area of the earthquake.

Hodgson & Bremner (1953) were the first to determine a fault plane solution for this event using first motion data from both horizontal and vertical instruments. Their solution (short dashes, Fig. 5) indicates movement along a fault striking 315° but dipping 71° to the north-east with a combination of reverse and strike-slip motion, a solution inconsistent with field observations. I redetermined the focal mechanism using the first motion data set shown in Fig. 5, which consists of Hodgson & Bremner's first motion observations for vertical instruments, additional first motions listed by the ISS (International Seismological Summary) for vertical instruments, and additional observations of vertical *P* and *PP* motions

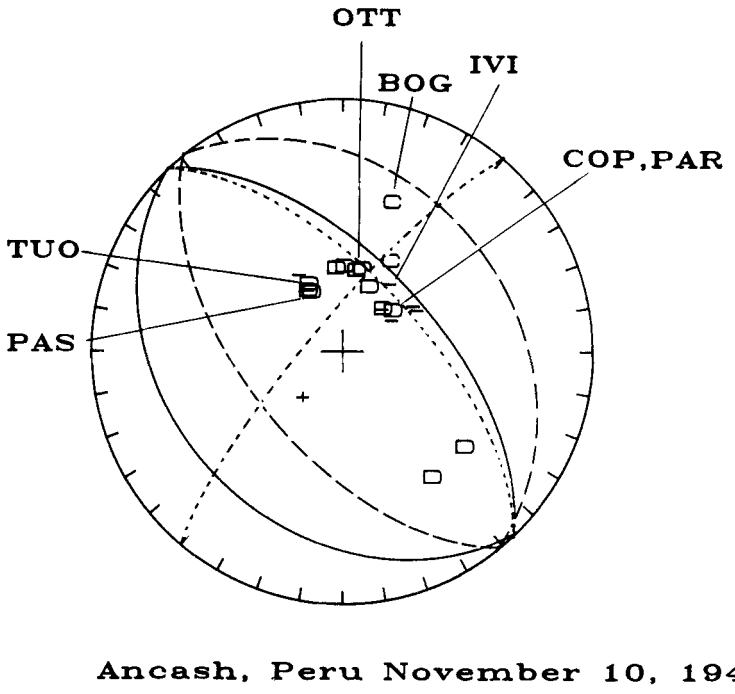

Figure 5. Focal mechanisms from first-motion data and surface faulting. First-motion data is plotted on a lower hemisphere projection, impulsive compressions and dilatations are denoted by C and D, emergent compressions and dilatations by + and −. The first-motion data consist of a subset of readings from Hodgson & Bremner (1953), readings from the International Seismological Summary, and motions read from original seismograms. The short dashes are the focal mechanism of Hodgson & Bremner (1953) (315, 65, −168), the solid lines the mechanism determined in this study (135, 30, −90), and the long dashes the mechanism obtained from observations of surface faulting (Silgado 1951) (140, 58, −90). Stations used in the waveform modelling are indicated by their three letter codes where PAS = Pasadena, California, TUO = Tucson, Arizona, OTT = Ottawa, Canada, IVI = Ivigtut, Greenland, COP = Copenhagen, Denmark, PAR = Paris, France. Note that BOG (Bogota, Columbia) was not modelled but its first motion polarity is discussed in the text.

read from original seismograms. A Jeffreys–Bullen earth model was used to calculated take-off angles.

The best fit to the data (Fig. 5, solid lines) is a mechanism with strike of 135° and dip of 30°, if pure dip-slip motion is assumed. This solution is similar to one obtained by Suárez *et al.* (1983) and the strike is within 5° of the strike of the surface faulting. It is important to note that the first-motion data could be fitted equally well with solutions with rakes of −40° to −120° and dips of 25° to 65° if the strike of the nodal plane is allowed to vary up to 45° from the strike of the observed surface-faulting.

Fig. 5 also shows the focal mechanism (long dashes) suggested by Silgado's observations of surface faulting. This mechanism is not consistent with the observed compressional first motion at Bogota (BOG, Fig. 5).

4 Waveform modelling

Requests for seismograms from seismograph stations around the world that were operating in 1946 and a search of seismogram archives in the United States yielded a collection of

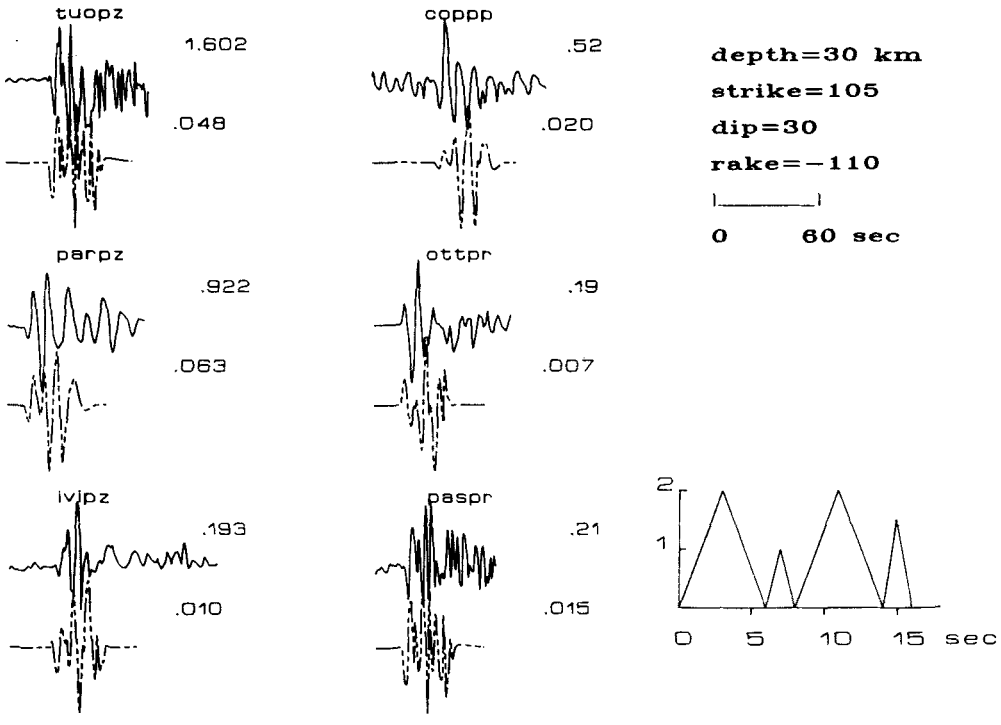

Figure 6. Observed (solid line) and synthetic (dashed line) seismograms of the Ancash earthquake for a focal depth of 30 km, a strike, dip and rake of 105°, 30°, −110°, respectively, and the source–time function indicated at lower right. The numbers to the right of each seismogram represent the maximum amplitude of the trace in centimetres. The synthetic seismograms were generated for a source with moment of 1×10^{18} N m^{-1}, therefore the moment is obtained by dividing the observed amplitude by the synthetic amplitude and multiplying by 1×10^{18} N m^{-1}. Station codes are the same as for Fig. 5. pz = vertical *P*, pr = radial *P*, sh = transverse *S*, pp = *PP* phase.

seismograms for six stations (Figs 5, 6). The limited focal-sphere coverage provided by these stations necessitated the modelling of radial *P*, transverse *S*, and *PP* phases in addition to vertical *P*. Vertical and radial *P* and transverse *S* were modelled for stations at epicentral distances of 50°–90° and a *PP* phase at a distance of 96°. The *PP* phase was Hilbert transformed using a technique outlined by Choy & Richards (1975) and Lynnes & Ruff (1985) before modelling. The forward modelling technique follows the method of Langston & Helmberger (1975).

A detailed description of near source crustal structure is not available, so the average *P*-wave velocity was assumed to be 6.0 km s^{-1} above the source and 6.8 km s^{-1} below the source for focal depths less than 20 km. For focal depths greater than 20 km the average *P*-wave velocity above the source was assumed to be 6.4 km s^{-1}. *S*-wave velocities were assumed to be $1/\sqrt{3}$ times smaller than the *P*-wave velocities. Uncertainties of ±0.2 km s^{-1} in these velocities would give an uncertainty of about ±2 km in focal depth. Receiver crustal structure was assumed to be a single layer with *P*-wave velocity of 6.0 km s^{-1}.

An attenuation operator, t^*, of 1.0 s was used for radial and vertical *P*, 4.0 s for transverse *S*, and 2.0 s for *PP*. The use of frequency dependent t^*'s such as those suggested by Anderson & Given (1982), Choy & Cormier (1986), and Der, Lees & Cormier (1987) would cause a minor trade-off between source duration and attenuation operator. This should not

affect the long-period estimate of moment, but the estimate of fault length might increase by 10 per cent. Geometrical spreading factors were taken from Kanamori & Stewart (1976) with the factor for the *PP* phase computed from the formula given by Lynnes & Ruff (1985).

Most seismograms studied were recorded on instruments with seismometer and galvanometer periods of 5–12 s (Table 2) and exhibited smooth waveforms (i.e. stations PAR, COP, Fig. 6). Seismograms recorded at Pasadena (PAS) and Tucson (TUO), however, were recorded on instruments with broadband-type responses (Table 2) and showed more complex waveforms (Fig. 6).

Table 2. Instrument constants

Station	Component	Seismometer period (s)	Galvanometer period (s)	Magnification
COP	Z	8.5	11.6	590
IVI	Z	4.9	–	200
	H	8.8	–	190
OTT	Z	1.0	48.0	500
	H	12.0	–	300
PAR	Z	12.6	12.6	1000
PAS	Z	1.0	90.0	2000
	H	1.0	90.0	2000
TUO	Z	1.0	77.0	3000
	H	8.0	–	460

In this study, synthetic seismograms were first generated using the fault-plane solution from first-motion data, a trapezoidal source–time function with duration of 4 s, and a 30 km focal depth. The focal mechanism was then varied by ±45° in strike, ±40° in dip and ±50° in rake in 5° intervals in an attempt to match the first half-cycle of motion at all stations. Goodness of fit was determined by cross-correlation of the data with the synthetic.

Next I attempted to match the first two cycles of the waveforms by varying focal depths within the range of 30–40 km, focal depths suggested by Silgado (1951) and Hodgson & Bremmer (1953), while keeping the focal mechanism and source–time function constant. Although the initial part of the waveform was well matched at PAS and TUO (Fig. 6), I was unsuccessful at matching the first part of the waveform at European stations, even if the source duration or focal mechanism were varied. I next tried focal depths in the range of 6–30 km and found that a focal depth of 15–17 km matched the waveforms at the European stations much better (Figs 7, 8). This focal depth is consistent with the study of Suárez *et al.* (1983) who found that earthquakes occurring at elevations greater than 3000 m in the Andes had focal depths ranging from 14 to 20 km.

After fixing the focal depth at 15 km, the focal mechanism was varied to match the first two cycles of the waveforms. The mechanism that best fitted the waveforms was: strike 105° ± 20°, dip 30° ± 10° SW, rake −100° ± 10° (Fig. 9). This is similar to the mechanism obtained from first motion studies (Fig. 9). The sensitivity of the waveform shape to dip is demonstrated in Fig. 10. At a dip of 20° the synthetic waveforms underestimate the amplitudes of the first *P*-wave troughs. At a dip of 40° for the synthetic waveforms overestimate the amplitudes of the first *P*-wave troughs and mismatch the *S*-wave shape.

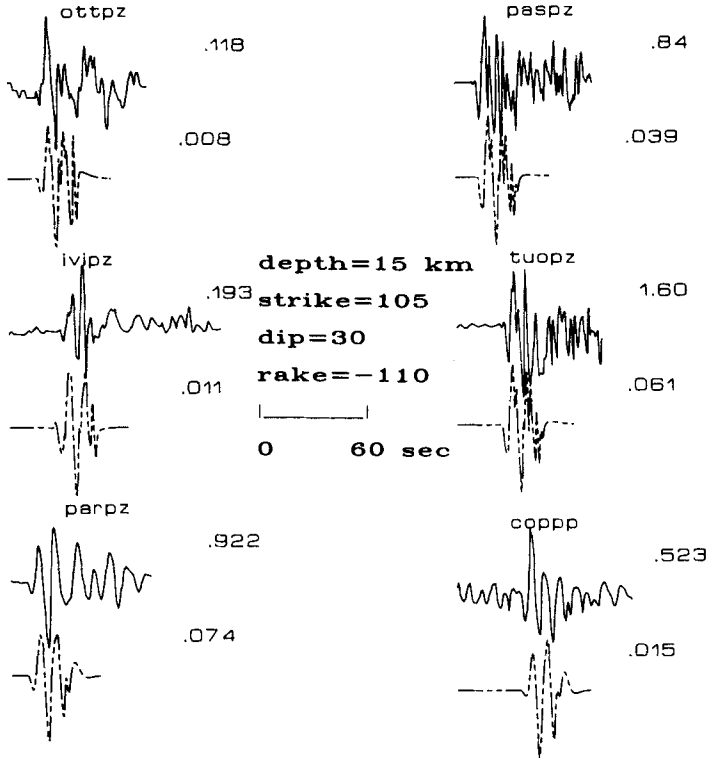

Figure 7. Observed and synthetic seismograms of the Ancash earthquake for vertical *P* and *PP* phases with a focal depth of 15 km. Strike, dip, rake, and source–time function are the same as in Fig. 6.

Finally the entire waveform was modelled to obtain the source–time function shape. Waveforms at European stations were well matched by a source–time function composed of two trapezoids, each of 6 s in duration, separated in time by 2 s. To match the broadband stations, however, a more complicated source–time function consisting of four triangles (two of 6 s duration, two of 2 s duration; Fig. 6) was required (Figs 7, 8). This function also matched some of the subtle features of the European waveforms.

It is probable that some of the waveform complexity seen at the broadband stations may be due to receiver structure or source structure or that the use of a constant attenuation model to generate synthetics for the broadband stations is not appropriate. Nevertheless, all waveforms suggest that the earthquake had a multiple source–time function. It is possible that Silgado (1951) mistook changes in the waveform shapes that are related to the rupture complexity for depth phases, causing an overestimation of focal depth.

It is not surprising that the earthquake was best modelled by a multiple source–time function when one considers the complexity of the local geology. The topographic expression of the fault scarp suggests that the fault is either youthful and/or that earthquakes along the fault have a long recurrence time. Thus the fault itself may have a complex, rough fault-plane. One eyewitness account of ground motion in the epicentral area (Silgado 1951) suggests that there were two large peaks in ground motion during the earthquake (e.g. the observer was violently thrown to the ground twice during the earthquake) which would be consistent with the two large peaks observed in the source–time function.

The average moment obtained from weighting individual moment estimates from the

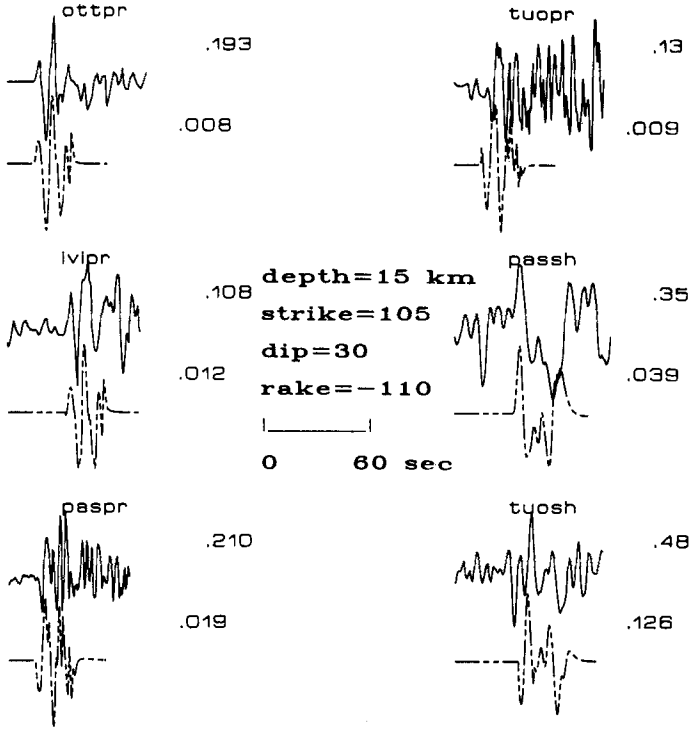

Figure 8. Observed and synthetic seismograms of the Ancash earthquake for radial *P* and transverse *S* with a focal depth of 15 km.

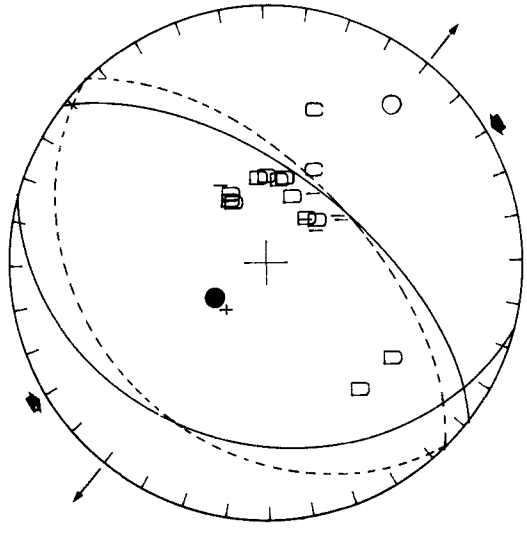

Figure 9. Focal mechanisms from waveform modelling of the Ancash earthquake. The solid line is the solution obtained from forward modelling. The dashed line is the mechanism from first-motion data. Average *P* and *T* axes of these solutions are denoted by the solid and open circles, respectively. Thin arrows indicate the average direction of maximum extension, bold arrows the direction of motion of the subducting Nazca plate in northern Peru (Stauder 1975).

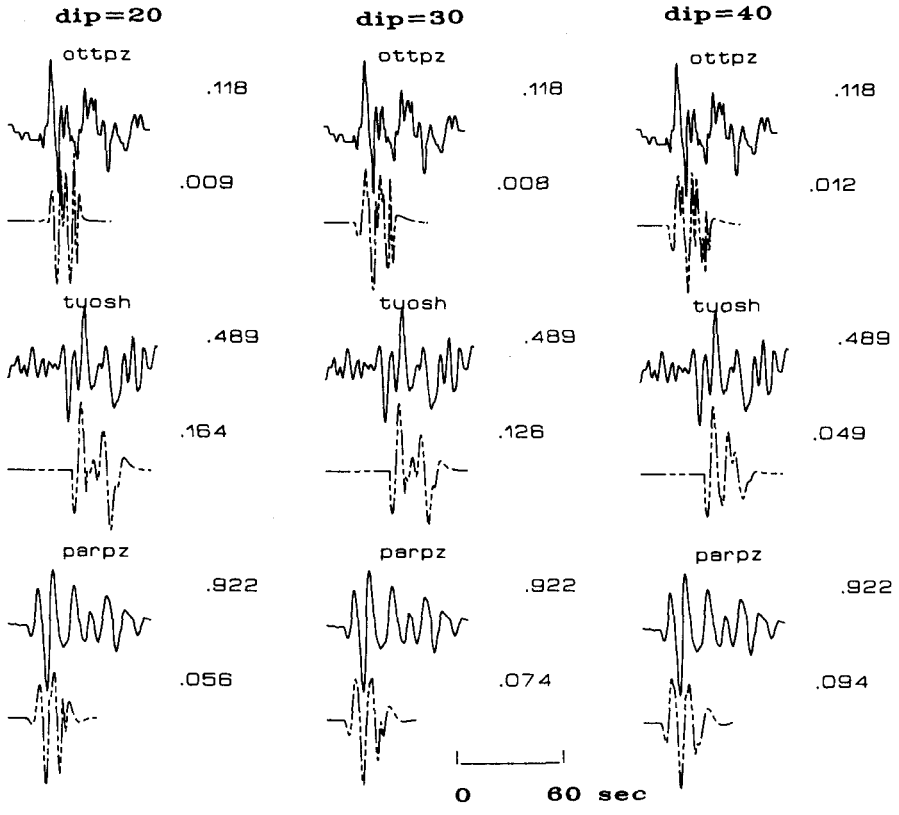

Figure 10. Sensitivity of seismogram shape to fault dips of 20°, 30°, and 40° for three stations. Strike, rake, and source–time function are the same as in Fig. 6. The focal depth is 15 km.

forward modelling by the fit between the data and synthetic was 1.7×10^{19} N m^{-1} (1.7×10^{26} dyne cm^{-1}). The highest moment estimates at individual stations were obtained for the broadband stations. The average moment (1.7×10^{19} N m^{-1}) corresponds to a moment–magnitude of 6.8 (Hanks & Kanamori 1979).

Unilateral rupture length can be estimated from $t_c = L/v$ (Kanamori & Stewart 1976), where t_c is the rupture time, L is the rupture length, and v is the rupture velocity, assumed to be 3.5 km s^{-1}. The total rupture time was estimated to be the same as the sum of the rise times of the individual triangles that made up the source–time function (8 s). This gives a rupture length of 28 km.

Using the relationship $M_0 = \mu A \bar{s}$, where M_0 is the seismic moment, A is the fault area (length × width, 28 × 30 km), and μ is the shear modulus, an average slip, $\bar{s}$, of 61 cm is obtained. This value is lower than the observed maximum slip of 1–3.5 m along individual fault segments. As mentioned previously it is not possible to deduce the average slip from Silgado's measurements. In light of the complexity of faulting, it is probably wrong to assume a planar, rectangular fault model to determine average slip. It is also possible that, although faulting began at a depth of 15–17 km, most slip was confined to shallower depths, thus decreasing the fault area and increasing the average displacement.

Although both moment and magnitude estimates suggest the earthquake was not as large as some recent normal fault-events in the western United States (Table 1), damage and loss of life was severe. This may in part be due to poor building construction, greater population

density, and the rugged topography of the Ancash region, which may have served to focus energy from the earthquake. The shallow dip of the rupture may also have played a role in ground shaking.

5 Discussion

Seismologically determined fault dips suggest that the Ancash earthquake occurred along a low-angle (30° ± 10° dip) normal fault that may represent an older reactivated thrust fault since nearby thrust faults are observed to tip 25°–35° at the surface (Heim 1949).

The presence of normal faulting in the Andes, a region of predominantly compressional tectonics, has been attributed to the effect of elevation on the stress field (Dalmayrac & Molnar 1981; Suárez *et al.* 1983). If horizontal compressive stress exceeds vertical stress (low elevations), thrust and reverse faulting exists. If vertical stress exceeds horizontal compressive stress (high elevations), normal faulting results. Thus we observe active reverse faulting 100–200 km south-east and north-east of the Ancash area (Suárez *et al.* 1983) at elevations near 1000 m, and normal faulting at 4000 m at Ancash.

Note that although the strike of the average *P*-axis for the earthquake (Fig. 9) aligns well with the average direction of subduction of the Nazca plate in northern Peru of N60°E (Stauder 1975), it is nearly vertical in orientation. The average *T*-axis (Fig. 9), however, is nearly horizontal and strikes (N40°E) within 20° of the average subduction direction. The average direction of maximum extension during the earthquake is also at an angle of 100° from the strike of the older thrust faults in the region (N60°W), and it seems logical that the rupture occurred along these older pre-existing zones of weakness since they are favourably orientated with respect to the present stress regime. If such a favourable orientation of maximum extensional stress with respect to older thrust faults is prevalent in other parts of the high Andes, then seismic hazard evaluations in the Andes must consider the possibility that shallowly dipping thrust faults could be reactivated in normal fault earthquakes.

Normal faulting of Quaternary age has been observed in the Altiplano of southern Peru and northern Bolivia (Mercier 1981; Suárez *et al.* 1983) and in the Cordillera Blanca Yonekura *et al.* 1979; Dalmayrac & Molnar 1981; Schwartz *et al.* 1984). (Fig. 1). Mercier (1981) has described normal-fault movement along older thrust faults in the Altiplano, which indicate that Ancash-type earthquakes may occur in this region. At present, reactivated thrust faults have not been recognized along the Cordillera Blanca, located 60–70 km south-west of the Ancash earthquake.

The Cordillera Blanca fault-zone extends for about 210 km, striking N40°W, dipping to the south or south-west with a pitch of 70°–90° (Dalmayrac & Molnar 1981); an orientation strikingly similar to the orientation of surface faulting in the Ancash earthquake. The Cordillera Blanca fault zone, however, is west of the Ancash fold and thrust belt region, and thrust faults are not observed to parallel the traces of normal faults at the surface.

Evidence for repeated movement is clearly seen in the topographic expression of the Cordillera Blanca fault zone. Slip rates of 2 mm yr^{-1} over the last 13 000–14 000 yr have been documented by trenching (Schwartz *et al.* 1984). This is in contrast to the Ancash fault zone where local topography suggests that either slip rates are much lower than those along the Cordillera Blanca fault zone and/or that normal fault movement has only recently begun. Until more subsurface information in the Cordillera Blanca region is available, one cannot rule out the possibility that normal faults in the region represent reactivated thrust faults.

The low angle nature of faulting during the Ancash earthquake contrasts with large

normal-fault earthquakes (1954–present) in the western United States which have occurred on faults dipping 50°–70° (Doser 1985, 1986; Doser & Smith 1985). The Ancash faulting is similar to low-angle faults seen on seismic reflection profiles throughout the western United States (Anderson, Zoback & Thompson 1983; Smith & Bruhn 1984), to the faults that developed in the western United States prior to the inception of Basin and Range faulting (Zoback, Anderson & Thompson 1981), and to low-angle normal faulting observed in the Aegean region (Jackson & McKenzie 1983; Eyidoğan & Jackson 1985).

6 Conclusions

The Ancash earthquake occurred along a normal fault that dips 30° ± 10° at depth. The close association of surface faulting with older thrust-faults suggests reactivation of an older thrust fault during the earthquake. Waveform modelling indicates that the earthquake began at a focal depth of 15–17 km, rather than previously determined values of 30–40 km. The waveforms of the earthquake are best fit by a multiple source–time function that reflects the complex local geology and segmented nature of the surface faulting. The magnitude of the earthquake is estimated to be 6.3–6.9. The large loss of life and extensive damage caused by the earthquake may have been related to poor building construction, rugged topography, focusing of earthquake energy by the topography, or the shallow dip of the fault. Similarities between the surface faulting in the Ancash earthquake and normal faults observed in other parts of the high Andes suggest that seismic hazard evaluation in this region should consider the likelihood that normal faults may dip at low angles and that rupture may occur along pre-existing thrust faults.

Acknowledgments

I thank D. P. Schwartz for first bringing the Ancash earthquake to my attention, for providing me with a copy of A. Heim's paper on the geology of the Ancash region, and for the many helpful comments he has given me. M. R. Baker also offered comments and suggestions throughout this study. J. C. Pechmann kindly reviewed a preliminary draft of the paper. Comments by two anonymous reviewers and an Editor are also appreciated. The help of numerous people from around the world who provided seismograms for this study is greatly appreciated. Computer time for the waveform modelling was provided by the University of Texas at El Paso Department of Geological Sciences.

References

Anderson, D. L. & Given, J. W., 1982. Absorption band Q model for the earth, *J. geophys. Res.*, **87**, 3893–3904.

Anderson, R. E., Zoback, M. L. & Thompson, G. A., 1983. Implications of selected subsurface data on the structural form and evolution of some basins in the northern Basin and Range Province, Nevada and Utah, *Bull. geol. Soc. Am.*, **94**, 1055–1072.

Burchfiel, B. C. & Davis, G. A., 1972. Structural framework and evolution of the southern part of the Cordilleran orogen, western United States. *Am. J. Sci.*, **272**, 97–118.

Burchfiel, B. C. & Davis, G. A., 1975. Nature and controls of Cordilleran orogenesis, western United States: extension of an earlier synthesis, *Am. J. Sci.*, **275A**, 363–396.

Choy, G. L. & Cormier, V. F., 1986. Direct measurement of the mantle attenuation operator from broad-band P and S waveforms, *J. geophys. Res.*, **91**, 7326–7342.

Choy, G. & Richards, P., 1975. Pulse distortion and Hilbert transformation in multiply reflected and refracted body waves, *Bull. seism. Soc. Am.*, **65**, 55–70.

Cloud, W. K., 1956. Intensity distribution and strong motion seismograph results, Nevada earthquakes of July 6, 1954 and August 23, 1954, *Bull. seism. Soc. Am.*, **46**, 34–40.

Cobbing, E. J. (compiler), 1973. *Geologic map of the western Cordillera of northern Peru (south sheet)*, scale 1:500,000, Government of Peru.

Dalmayrac, B. & Molnar, P., 1981. Parallel thrusts and normal faulting in Peru and constraints on the state of stress, *Earth planet. Sci. Lett.*, **55**, 473–481.

Der, Z. A., Lees, A. C. & Cormier, V. F., 1987. Frequency dependence of Q in the mantle underlying the shield areas of Eurasia, III: the Q model, *Geophys. J. R. astr. Soc.*, **87**, 1103–1112.

Doser, D. I., 1985. Source parameters and faulting processes of the 1959 Hebgen Lake, Montana, earthquake sequence, *J. geophys. Res.*, **90**, 4537–4555.

Doser, D. I., 1986. Earthquake processes in the Rainbow Mountain–Fairview Peak–Dixie Valley, Nevada, region (1954–1959), *J. geophys. Res.*, **91**, 572–586.

Doser, D. I. & Smith, R. B., 1985. Source parameters of the 28 October, 1983, Borah Peak, Idaho, earthquake from body wave analysis, *Bull. seism. Soc. Am.*, **75**, 1041–1051.

Eyidoğan, H. & Jackson, J., 1985. A seismological study of normal faulting in the Demirci, Alasehir and Gediz earthquakes of 1969–70 in western Turkey: implications for the nature and geometry of deformation in the continental crust, *Geophys. J. R. astr. Soc.*, **81**, 569–607.

Flinn, E. A., 1965. Confidence regions and error determinations for seismic event location, *Rev. Geophys.*, **3**, 157–185.

Hanks, T. C. & Kanamori, H., 1979. A moment magnitude scale, *J. geophys. Res.*, **84**, 2348–2350.

Heim, A., 1949. *Observaciones geologicas en la region del terremoto de Ancash de noviember de 1946, Vol: jubilar*, Part. II, pp. 1–28, Soc. Geol. del Peru, Lima, Peru.

Hodgson, J. H. & Bremner, P. C., 1953. Direction of faulting in the Ancash, Peru, earthquake of November 10, 1946, from teleseismic evidence, *Bull. seism. Soc. Am.*, **43**, 121–125.

Jackson, J. & McKenzie, D., 1983. The geometrical evolution of normal fault systems, *J. struct. Geol.*, **5**, 471–482.

Kanamori, H. & Stewart, G. S., 1976. Mode of strain release along the Gibbs fracture zone, Mid-Atlantic Ridge, *Phys. Earth. planet. Int.*, **11**, 312–332.

Langston, C. A. & Helmberger, D., 1975. A procedure for modelling shallow dislocation sources, *Geophys. J. R. astr. Soc.*, **42**, 117–130.

Lynnes, C. S. & Ruff, L. J., 1985. Use of the *PP* phase to study the earthquake source, *Geophys. Res. Lett.*, **12**, 514–517.

Mercier, J. L., 1981. Extensional–compressional tectonics associated with the Aegean Arc: comparison with the Andean Cordillera of south Peru–north Chile, *Phil. Trans. R. Soc. A*, **300**, 337–355.

Richter, C. F., 1958. *Elementary Seismology*, W. H. Freeman, San Francisco, 768 pp.

Sanford, A. R. & Topozada, T. R., 1974. Seismicity of proposed radioactive waste disposal site in southeastern New Mexico, *Circular 143, New Mexico Bur. of Mines and Min. Resouces*, 37 pp.

Schwartz, D. P., Salazar, H., Felix, O., Santucci, H., Arnt, A., La Cruz, J. & Farfan, M., 1984. Late quaternary normal faulting, recurrence intervals, and slip rates along the Cordillera Blanca fault zone, northern Peruvian Andes (abstract), *EOS, Trans. Am. geophys. Un.*, **65**, 1082.

Silgado, E., 1951. The Ancash, Peru, earthquake of November 10, 1946, *Bull. seism. Soc. Am.*, **41**, 83–89.

Smith, R. B. & Bruhn, R. L., 1984. Intraplate extensional tectonics of the eastern Basin-Range: inferences on structural style from seismic reflection data, regional tectonics and thermal–mechanical models of brittle–ductile deformation, *J. geophys. Res.*, **89**, 5733–5762.

Stauder, W., 1975. Subduction of the Nazca plate under Peru as evidenced by focal mechanisms and by seismicity, *J. geophys. Res.*, **80**, 1053–1064.

Steinbrugge, K. V. & Cloud, W. K., 1962. Epicentral intensities and damage in the Hebgen Lake, Montana, earthquake of August 17, 1959, *Bull. seism. Soc. Am.*, **52**, 181–234.

Stover, C. W., 1985. Isoseismal map and intensity distribution for the Borah Peak, Idaho, earthquake of October 18, 1983, *U.S. geol. Surv. Open File Rep.*, **85-290**, 401–408.

Suárez, G., Molnar, P. & Burchfiel, B. C., 1983. Seismicity, fault plane solutions, depth of faulting, and active tectonics of the Andes of Peru, Ecuador, and southern Columbia, *J. geophys. Res.*, **88**, 403–428.

Wilson, J. J., Reyes, L. & Garayar, J., 1967. Geologia de los Cuadrangulos de Mollebamba, Tayabamba, Huaylas, Pomabamba, Carhuaz y Huari, *Bol. Serv. Geol. Min. Lima*, **16**, 95 pp.

Yonekura, N., Matsuda, T., Nogami, M. & Kaizuka, S., 1979. An active fault along the western part of the Cordillera Blanca, Peru, *J. Geogr.*, **88**, 1–19.

Zoback, M. L., Anderson, R. E. & Thompson, G. A., 1981. Cainozoic evolution of the state of stress and style of tectonism of the Basin and Range provinces of the western United States, *Phil. Trans. R. Soc. A*, **300**, 407–434.